

1 **3D models and structural analysis of rock avalanche: the**
2 **study of the deformation process to better understand the**
3 **propagation mechanism**

4 **C. Longchamp¹, A. Abellan¹, M. Jaboyedoff¹ and I. Manzella²**

5 [1]{Institute of Earth Sciences, University of Lausanne, Switzerland}

6 [2]{Department of Earth Sciences, University of Geneva, Switzerland}

7 Correspondence to: C. Longchamp (celine.longchamp@unil.ch)

8

9 **Abstract**

10 Rock avalanches are extremely destructive and uncontrollable events that involve a great
11 volume of material ($>10^6 \text{ m}^3$), several complex processes and they are difficult to witness. For
12 this reason the study of these phenomena using analogue modelling and the accurate analysis
13 of deposit structures and features of laboratory data and historic events become of great
14 importance in the understanding of their behavior.

15 The main objective of this research is to analyze rock avalanche dynamics and deformation
16 process by means of a detailed structural analysis of the deposits coming from data of 3D
17 measurements of mass movements of different magnitudes, from decimeter level scale
18 laboratory experiments to well-studied rock avalanches of several square kilometers
19 magnitude.

20 Laboratory experiments were performed on a tilting plane on which a certain amount of a
21 well-defined granular material is released, propagates and finally stops on a horizontal
22 surface. The 3D geometrical model of the deposit is then obtained using either a scan made
23 with a 3D digitizer (Konica Minolta vivid 9i) either using a photogrammetric method called
24 Structure-from-Motion (SfM) which requires taking several pictures from different point of
25 view of the object to be modeled.

26 In order to emphasize and better detect the fault structures present in the deposits, we applied
27 a median filter with different moving windows sizes (from 3x3 to 9x9 nearest neighbors) to
28 the 3D datasets and a gradient operator along the direction of propagation.

1 The application of these filters on the datasets results in: (1) a precise mapping of the
2 longitudinal and transversal displacement features observed at the surface of the deposits; and
3 (2) a more accurate interpretation of the relative movements along the deposit (i.e. normal,
4 strike-slip, inverse faults) by using cross-sections. Results shows how the use of filtering
5 techniques reveal disguised features in the original point cloud and that similar displacement
6 patterns are observable both in the laboratory simulation and in the real scale avalanche,
7 regardless the size of the avalanche. Furthermore, we observed how different structural
8 features including transversal fractures and folding patterns tend to show a constant
9 wavelength proportional to the size of the avalanche event.

10

11 **1 Introduction**

12 Rock avalanches, or Sturzstroms (Heim, 1932) are defined as an extremely rapid, massive,
13 flow-like motion of fragmented rocks derived from a bed-rock failure (Hungre et al., 2001).
14 Rock avalanches are events in which granular masses of rock debris flow at high speeds,
15 commonly with unusually runout (Corominas, 1996; Friedmann and Losert, 2003). A great
16 volume of material ($>10^6 \text{ m}^3$) is involved and the flowing mass can reach velocities in the
17 order of tens meters per second. They can travel long distances, in the order of kilometers and
18 cover an area over 0.1 km^2 (Hsü, 1975). They present a very high mobility and need to be
19 simulated with adapted frictional models (Hungre et al., 2001, Pedrazzini et al., 2012). Authors
20 proposed different possible causes, which could explain the high mobility of these
21 phenomena, such as the influence of the large destabilized volume (Heim, 1932; Hsü, 1975;
22 Scheidegger, 1973; Nicoletti and Sorriso-Valvo, 1991), the momentum transfer within the
23 rear and the front of the flowing mass (Van Gassen and Cruden, 1989; Manzella and
24 Labiouse, 2009), or the fragmentation of the spreading mass (Heim, 1932; Davies, 1982;
25 Davies and McSaveney, 1999; Locat et al., 2006). In order to understand the behavior of such
26 granular flows, laboratory scale experiments provide important information on their
27 propagation and on the parameters influencing their mobility, even if they reproduce idealized
28 conditions (Davies and McSaveney, 1999, 2003; McDougall and Hungre, 2004; Shea and van
29 Wyk de Vries, 2008; Manzella and Labiouse, 2008, 2009; Longchamp 2016). Dufresne
30 (2012) highlighted that substrate material with the least frictional resistance showed the
31 greatest response to granular flow, producing the longest runout. In their work, Andrade et al.
32 (2010) and Paguican et al. (2014) studied analogue flank collapse and highlighted that

1 hummocks can form horst and graben structures during lateral spreading. Several authors
2 proposed different parameters for the geometrical description of large landslides. One of the
3 most used is the Fahrböschung concept, which was introduced by Heim (1932) to estimate the
4 maximum runout of rock avalanches or landslides (Scheidegger, 1973; Hsü, 1975; Davies,
5 1982) and which is defined as the angle of the straight line connecting the head of the scar to
6 the end of the deposit.

7 The presence of faults and folds are common features on the surface of rock-avalanche
8 deposits. One of the best examples is the rock avalanche deposit of Socompa volcano
9 (Northern Chili). This deposit was widely studied before (Francis et al., 1985; van Wyk de
10 Vries et al., 2001; Kelfoun and Druitt, 2005; Shea and van Wyk de Vries, 2008) and presents
11 a well preserved morphology thanks to the local arid climate. A complex assemblage of
12 surface structures (normal faults, strike-slip faults, thrusts, ridges) is displayed on the surface
13 of the deposit. Van Wyk de Vries et al. (2001) showed that these structures incise deeply the
14 internal part of the deposit. The non-volcanic deposit of Blackhawk (California, USA) also
15 presents similar features (Shea and van Wyk de Vries, 2008) (Figure 1a) as well as the Frank
16 Slide in Alberta (Canada) (Cruden and Huger, 1986, 2011; Charrière et al., 2015). Features
17 perpendicular to the flow direction are mainly present in the distal part of the deposit and are
18 interpreted as the surface expression of the underneath topography. Reversibly, longitudinal
19 features on the proximal and the central part of the deposit are assumed to be morphological
20 features that were created during the process of avalanche propagation and deposition. It is
21 also interesting to highlight that similar features have been observed in other planets such as
22 in the Mont Olympus (Mars) (Figure 1b). Shea and van Wyk de Vries (2008) provided a
23 detailed map of this extraterrestrial Martian rockslide avalanche where it can be observed that
24 thrust faults are located in the front of the deposit and that are cut by strike-slip faults. Normal
25 faults are presented in the central part of the deposit. Although, these features occur during
26 the emplacement of the deposit, however, few studies focus on these deformational settings.
27 In their small-scaled experiments, Dufresne and Davies (2008) showed that lateral levees
28 developed where flows was parallel to the confining whereas compressional ridge formed in
29 response to declination in the front of the deposit.

30 In the present paper a detailed structural analysis is carried out based on data coming from
31 dedicated laboratory experiments and historic events in order to better understand the
32 deformation of these complex phenomena. Moreover, this research attempted to propose a

1 simple methodology to describe and map the features at the surface of the deposits in order to
2 provide information on the mobility of the rock avalanche.

3 **2 Experimental methods**

4 The first step of this study consisted in carrying out laboratory experiments in order to study
5 the influence of a series of parameters on the features and structure of granular flow deposits.
6 The experimental setup (see Figure 2) consisted in a simple aluminum slope geometry
7 composed of two distinct parts: a 90 x 70 cm slope with an inclination (α) which can be
8 precisely modified, connected with a curved part to a 120 cm long horizontal surface.
9 Furthermore, the experimental setup also includes a box (11 x 8 x 7 cm) where the loose
10 material is enclosed at the beginning of the experiment. This box, separated from the main
11 set-up, can be leant against the slope and quickly separated from it by means of a retractile
12 jack. This allows placing a precise quantity of granular material on the slope and releasing it
13 avoiding any vibrations. Experiments then consist letting the mass propagating without lateral
14 confinements till it reaches a complete stop (Figure 2). As loose material is used, partial
15 mixing of grains is observed. The fragmentation of layers is not taken into account in this
16 study.

17 Two different materials were used for the experiments: a) the first type of material
18 corresponds to angular and calibrated carborundum sand (SiC, density = 3.21 g/cm³) with
19 three different grainsizes (Table 1). The choice of carborundum was made in order to avoid
20 the characteristic electrostatic effects that have been often observed in granular flow
21 experiments and that are not present in real events (Iverson and Denlinger 2001; Manzella,
22 2008). Furthermore, the angular shape of this type of material has close resemblances with
23 natural material; b) the second material corresponds to colored sands of similar grainsize
24 (Table 1). The choice of this material was driven by the need of observing the evolution of the
25 initial stratigraphy, i.e. to analyze the deposit stratigraphy (given by different layers of
26 different colors) during motion and emplacement of the mass.

27 The slope and the surface of deposition were artificially roughed by adding sandpaper, also
28 made of carborundum sand, where the grain diameter has been varied. The basal friction μ
29 angle for each sandpaper was estimated by means of a dynamometer and the results are given
30 in Table 2.

1 No scaling calculations were applied for this work but we based our value for the slope,
2 height of fall grainsize for the laboratory on work of Shea and van Wyk de Vries (2008). All
3 the experiments were carried out with a constant volume within the same experiment (400cm^3
4 $< V < 500\text{cm}^3$) and same height of fall for the granular material (50 cm). The runout of dry
5 granular flow is influenced by the slope angle: the runout distance is greater for higher slope
6 angle (Longchamp, 2016). For this study, a slope angle of 40° is chosen to better compare the
7 results.

8 The experiments were recorded by a high speed camera (30 fps for a resolution of 640x480),
9 the final deposit was scanned by a 3D digitizer (Konica Minolta vivid 9i micro-Lidar with a
10 resolution of 30'000 points per point cloud, Figure 2) and photographed. Finally a transparent
11 separation is placed carefully along the major longitudinal section and the material on one
12 side is removed so that it is possible to observe the internal structure of the mass. In order to
13 observe the repartition of the colored sand grains within the deposit, sand grains were counted
14 at crucial sections along the deposit. For each measurement, a section of 0.2 cm length and a
15 height corresponding to the thickness of the deposit was determined. Into this section, the
16 number of colored grains was manually counted. This gave further information on the
17 different regimes affecting the flow and allowed to better constrain the different part of the
18 deposit that are affected by different regime. Ten measurements were made along the deposit
19 and cumulated.

20 In order to have significant results, three experiments are carried out with equal initial
21 conditions.

22

23 **3 Methodology**

24 As mentioned above, during the propagation, the motion of the granular mass is recorded by a
25 high-speed camera in order to analyze the deformation and spreading during the flow. Once
26 the mass stopped, the first step was to take pictures of the deposit in order to study and
27 inventory the visible longitudinal and transversal features on the surface. The acquisition of
28 3D dataset was made using either a laser scanner (Konica Minolta vivid 9i micro-Lidar) either
29 a photogrammetry technique, named Structure-from-Motion (SfM) (Westboy, 2012). The
30 laser scanner technique is useful to scan the deposit resulting of the propagation of
31 carborundum sand but the density of points is quite low (30'000 points per point cloud) (see

1 Figure 3b). Moreover, the setup is quite difficult to install and the data are long to process.
2 SfM differs fundamentally from conventional photogrammetry, in that the geometry of the
3 scene, camera positions and orientation is solved automatically without the need to specify a
4 priori a network of targets which have known 3-D positions (Westboy, 2012). Instead, these
5 parameters are solved simultaneously using a highly redundant, iterative bundle adjustment
6 procedure, based on a database of features automatically extracted from a set of multiple
7 overlapping images (Westboy, 2012). Structure from Motion is a simple technique requiring
8 little material and is cheaper compare to Lidar. The density of points is high (1'000'000
9 points per point cloud). This density of points allows identifying finer features on the deposit.
10 The main disadvantage of this technique is that the post processing of the data is sensitive to
11 all variation in the images. Therefore, SfM cannot be applied to experiments with
12 carborundum sand as the grains reflect the light with different intensity according to where
13 the pictures is taken and it could only be applied to the colorized sand deposit (Figures 4). To
14 summarized, no problems of reflection were observed when using carborundum when it is
15 scanned by a Lidar. On the contrary, when using photogrammetry on the carborundun sand,
16 the resulting point cloud is noisy. For this reason, we applied the photogrammetry to the
17 colored sand. The advantage of the photogrammetry with the colored sand is that we have a
18 colored point cloud and way more point compare to the Lidar. On the other hand, acquisition
19 with the Lidar allowed us to have point clouds of all experiments carried out with
20 carborundum. Thanks to the use of different filtering techniques and operators, we were able
21 to highlight the structural fingerprints on the deposit surface. This computational work aimed
22 to highlight the features that cannot be observed by a naked eye, as follow:

23 (a)Application of a median filter technique

24 Data acquisition using 3D digitizer leads or SfM to a “noisy” surface in which the features to
25 be detected are masked due to the scattering of the 3D points around the real surface (Figure
26 5a). To remove the noise, smoothing filters are used in preprocessing steps (Gonzalez and
27 Woods, 2002; Pugazhenti and Priya, 2013). After Gonzalez and Woods (2002), order-statistic
28 filters are nonlinear filters whose response is based on ordering the pixel contained in the
29 image area encompassed by the filter, and then replacing the value of the center pixel with the
30 value determined by the ranking value. The first step was to remove the noise using a 2-D
31 median filtering using different window sizes (Figures 5b and 5c).

1 (b)Application of a gradient operator

2 Once the noise was removed of the dataset obtained with 3D digitizer or SfM, a numerical
3 gradient is applied to the filtered dataset. The gradient was applied along two directions to
4 highlight changes in the slope orientation as proposed in Kumar et al. (1996) and Gonzalez
5 and Woods (2002). First, we calculated the gradient parallel to the flow direction (along the x
6 axis), and then the gradient perpendicular to the flow direction (along the y axis):

$$7 \quad \nabla F = \frac{\partial F}{\partial x} i + \frac{\partial F}{\partial y} j \quad [3]$$

8 The objective of detecting variation of the gradient along x and y is to highlight any
9 preferential orientation. The detected variations of the slope are interpreted as structures
10 developed on the surface of the deposit. Once the gradient operator is applied, the point cloud
11 is imported in the IMInspect module of Polyworks software (InnovMetric)

12 (c)Comparison with real case

13 In order to extend the proposed workflow to a real case study, we decided to apply the
14 filtering gradient operator techniques to the well-known Frank Slide event (Alberta, Canada).
15 This deposit presents several geometrical features, which are mainly longitudinal and
16 perpendicular to the flow direction (Longchamp et al., 2011; Charrière et al., 2015).

17

18 **4 Results**

19 **4.1 Results I: Experiment description**

20 **a) Visual inspection from photography**

21 Laboratory experiments were carried out with different volumes, grainsizes and using
22 different basal roughness but only the finer grainsize (F120) presented visible features on the
23 surface of the deposit as shown in Figure 6a. Three distinct sets of features can be observed in
24 this figure: inverse faults, normal faults and strike-slip faults. The first set, the inverse faults,
25 is composed of long features, perpendicular to flow direction following the outline of the
26 front with a tendency to become parallel to the global flow direction at the lateral margins
27 (green lines on Figure 6b). The second set is formed by thin normal faults located at the rear

1 part of the deposit and perpendicular to the flow direction (red lines on Figure 6b). Two
2 different sets of strike-slip faults can be observed. The first one is composed of short and thin
3 features parallel to the flow direction and present at the front of the deposit. These features
4 can be observed cutting the inverse faults at the frontal part and cutting the normal faults at
5 the rear part. The second one is made of strike-slip faults parallel to the flow direction and are
6 present at the lateral margins of the deposit.

7 **b) Visual inspection from high speed video**

8 In high-speed video, propagation of the mass is easily observable. Sand of three different
9 colors was used and was poured in the starting box as follow: 150 ml of red sand as the lower
10 layer, 150 ml of grey sand as intermediate layer and finally, 150 ml of green sand. The slope
11 is made rough with the finer substratum ($\mu=33.40^\circ$) and the slope angle is 40° . Once the trap
12 is open and the material is free to flow, all the layers are stretched under an extensional
13 regime. Once the frontal part reach the horizontal surface, its velocity is decreased. As the
14 mass continues to flow on the slope, the front is compressed and pushed forward. The mass is
15 finally stopped once all the mass reaches the horizontal surface. The high-speed video is
16 available in supplemental material.

17 **4.2 Results II: point cloud processing**

18 Figure 7 shows the results of the point cloud processing for all the simulations, i.e. using three
19 grainsizes (F10, F36 and F120) on the different substrata (Table 2). For the coarser grainsize
20 (F10), the application of the different filters and operator techniques has not highlighted any
21 remarkable features. As the amplitude of the features is less than one millimeter, the coarser
22 grainsizes are too large to capture deformation. The only noticeable thing is that the shape of
23 the deposit became more ellipsoidal with a decreasing basal roughness and confirmed the
24 observation made by Dufresne et al. (2016) that substrates shaped the morphology of rock
25 avalanches. For the medium grainsize (F36) the filters clearly highlighted a series of features
26 perpendicular to the flow direction. In Figure 7, it also can be observed that the basal friction
27 influenced the formation of features at the deposit surface. The density of these features
28 increases with the reduction of the basal roughness. In this case filters allowed detecting
29 features that were not visible on the pictures alone.

1 As it can be observed on Figure 7, the gradient along Y can be considered as an efficient
2 manner for the observation of the different features affecting the surface of the deposits.

3 Using this operator, we observed that the back of the deposit presents high concentration of
4 small features parallel to the flow direction. Figures 8a and 8b present the back of an analogue
5 deposit (F120 on the finest substratum) after the point cloud processing and imported in the
6 IMInspect module of Polyworks software (InnovMetric). Two different sets are observable:
7 one perpendicular to the flow direction and the second composed of features parallel to the
8 flow direction and cutting the first set (Figure 8). The first set was observed with naked eye
9 whereas the second set is only recognizable after post processing.

10 **4.3 Frank Slide**

11 The same visual inspection and filtering methods were applied to the Frank Slide deposit.
12 Figure 9a is the result of the interpretation of the features mapped directly on the DEM and
13 Figure 9b is the result of the application of a gradient along the flow direction. The main
14 features observed in the DEM are also recognizable on the gradient map, but a series of
15 structures that are masked on the DEM image can be identified in the gradient image. Figures
16 9c and 9d show a zoom of the deposit after the filtering. In the Figure 9c, features parallel to
17 the flow direction are clearly identifiable whereas in the Figure 9d, the features are parallel to
18 the flow direction.

19 **5 Discussion**

20 Our workflow has allowed the identification of three distinct sets of features on the analogue
21 granular flow deposit. Those features are important marks of the processes happening during
22 the flow and the emplacement of the mass and could be crucial in improving our
23 understanding of the dynamics and the reasons of the high mobility of rock avalanches. The
24 inverse faults are well marked on the deposit front, reflecting the compression affecting the
25 frontal part of the mass. Inverse faulting system appears as soon as the frontal part of the
26 granular mass hits the surface of deposition and its velocity starts to slow down. Then, the
27 granular material accumulates on the rear part, pushing forward and compressing the frontal
28 part of the deposit. Normal faults were formed during an extensional regime, when the mass
29 was stretched during the flow and by the pulling of the frontal part of the mass. Strike-slip
30 faults are present at the front of the deposit. As the mass is thinner at the margins and
31 consequently the velocity decreases while the central part of the mass is still on motion letting

1 strike-slip faults appear at the lateral margins of the deposit. The strike-slip faults are the
2 expression of the shearing occurred during the deceleration of the mass (Shea and van Wyk
3 de Vries, 2008).

4 Thanks to the application of the filtering on analogue deposit 3D datasets, the structures
5 observed during the laboratory experiments were highlighted. One advantage is that the use of
6 filters allows detecting features for the finest sand (F120) and also for the medium one (F36),
7 for the totality of the basal roughness. The fact that no features are observed for the coarse
8 grainsize (F10) can be explained by the fact that the size of features is of the same order of
9 magnitude that the size of the grains. The gradient along Y gave the best results since it
10 allowed detecting long inverse faults at the front and some normal faults at the back.
11 Moreover, the study of the result of the Y-gradient with the Polyworks software shows that
12 the normal faults at the back are numerous and cut by strike-slip faults (Figure 8). These
13 strike-slips faults appear after the extensional regime, during the shearing caused by the mass
14 deceleration. These features give crucial information for the mobility of the mass and are not
15 detectable with naked eye.

16 Thus, different regimes were distinguished: the compressional, the extensional and the
17 shearing regimes. Based on this assumption we could deduce the behavior of the granular
18 mass looking at the high-speed camera snapshots as shown in Figure 10. This figure
19 represents for each time step on one side the movie snapshot and on the other the
20 interpretation related to it. In order to improve the clarity of the observation made, no
21 distinction between the layers is made for the interpretation. Two main regimes are detected,
22 the compressional, outlined on the interpretation with dots and the extensional one, outlined
23 with lines. Following the time steps shown in Figure 10 we can then observe:

24 Step 1: Once the trap is open, the front of the granular material starts to flow. Because of the
25 release geometry, layering occurred during the flow.

26 Step.2: All the mass behaves under an extensional regime through all directions during the
27 time preceding the deposition of the granular flow.

28 Step.3: Shortly after the free flow, the front of the mass hits the surface of deposition,
29 decreasing suddenly its velocity. Two different tensional states are found at this step.
30 While the mass on the slope it is under high extensional regime the front starts to be
31 under compressional regime as it hits the surface of deposition and the velocity starts
32 to slow down. In addition to that, at this stage of the experiment, we start observing

1 one additional aspect characterizing the green layer. In fact we can first distinguish a
2 part of the green mass flowing which behaves differently from the rest of the mass.
3 This part is likely to constitute the rear zone in the initial configuration of this layer.
4 Moreover, at this step, it can be observed that the basal red layer has a lower velocity
5 than the other layers, as it is less visible in the picture.

6 Step.4: At this step, the back is still under an extensional regime and the front under a high
7 compressive regime as the flowing material continues to push it forward. The rear
8 part of the green layer is faster than the underneath layers.

9 Step.5: The gray and green layers continue to be pushed by the main body of the mass.
10 Consequently, shearing appears at the front. As the red layer is the basal layer, it is
11 slowed by friction. As the margins of the mass are thinner compared to the central
12 part, their velocity is less important and shearing takes place. Simultaneously, the
13 rear part of the green layer is faster compare to the lower layers and hits the mass
14 already deposited.

15 Step.6: The back of the mass continues to flow and is still under extensional regime, pushing
16 the front forward. At this step, shearing is still important at the margins and at the
17 front.

18 Step.7: The front is stopped and the rest of the material still on the ramp finishes to flow down
19 creating the shearing observed at the back of the deposit, cutting the normal faults.

20 Step.8: The mass is finally stopped. It is interesting to highlight that the original stratigraphy
21 is conserved and observable at the front.

22 The profile AA' along the flow direction was obtained for the laboratory experiment (Figure
23 11a). This profile allowed observing the internal part of the mass and the depth of the main
24 features. Figure 11b gives the image of the section along the AA' line shown in Figure 11a
25 and the Figure 11c is its interpretation. In Figure 11c, inverse faults are visible at the front
26 (well-marked by red grains in the Figure 11b) whereas normal faults are visible at the rear
27 part of the deposit. In this figure, it can be observed that the center of the mass is mainly
28 composed of green sand, confirming that the rear part of the green layer in Figure 10 hits the
29 mass already present on the surface of deposition (steps 5-7 in Figure 10). When this mass
30 hits the deposit, it probably increased the compression explaining the numerous inverse faults
31 present at the front (Figure 11c).

1 To confirm what observed the number of colored sand grains has been counted along the
2 central section of the deposit, as reported on Figure 12. Results confirmed what showed by
3 Figure 11b and 11c with the identification of an extension-dominated area in the rear and a
4 compression dominated area in the front. The rear part of the deposit corresponds to the
5 extension-dominated area. This area is mainly composed of red sand whereas few green
6 grains were observed. In the contrary, the central part of the deposit is mainly composed of
7 green sands. Indeed, this part corresponds to the rear part of the deposit that hit the mass
8 already deposited (Figure 10). The frontal part of the deposit corresponds to the compression-
9 dominated area. The compression caused by the impact of the green layer of grains in the
10 central part pushed part of the lower layer (red) further on the front and towards the surface
11 creating the inverse faults also showed in Figure 11c. Indeed, in this frontal part, we can
12 observe that the amount of red sand increases.

13 Because of the position of the profile, the red layer is not clearly visible at the front of Fig.
14 11b and 11c but the conservation of the initial stratigraphy is observable in the Fig. 11a. The
15 fact that the initial stratigraphy is preserved in the final deposit it is relevant since this feature
16 has been already detected in several real cases and it has been recognized as one of the main
17 ones characterizing rock avalanche deposit (Erismann, 1979, Manzella and Labiouse, 2013).
18 Thanks to the film analysis we could then relate some propagation mechanisms with the
19 consequent preservation of the initial stratigraphy in the final deposit and this could give an
20 insight in the dynamics of real rock avalanches.

21 This study confirmed that the structures are not randomly distributed. As it can be observed in
22 Fig. 6, the inverse faults are present a the frontal part of the deposit, which correspond to the
23 compression-dominated area. Normal faults are mainly observed at the back of the deposit
24 (Figure 6 and Figure 8), which correspond to the extension-dominated area. Finally, strike-
25 slipe faults are observed at the back and at the margins of the deposit (Figure 6 and Figure 8).
26 These repartition was also observed in the Blackhawk deposit (Figure 1a) and in a Martian
27 deposit (Figure 1b) (Shea and van Wyk de Vries, 2008). Based on the study of the DEM of
28 Frank Slide deposit and with the filtering technique, the same repartition of the features was
29 observed (Figure 9).

30 **6 Conclusion**

31 The use of 3D dataset, accurate visual inspection and a performing filtering method give
32 crucial information on the motion of granular mass. To summarized:

- 1 1. Three families of faults were highlighted on the surface of the deposit: normal faults,
2 inverse faults and strike-slip faults. We also highlighted that strike-slip faults are
3 present at the back of the deposit.
- 4 2. The identification of the different features allowed identifying three regimes during
5 the propagation of the mass: extensional, compressional and shearing. The extension
6 to real cases of the interpretation of the motion of the granular mass based on
7 laboratory experiments is comforted by the fact that the initial stratigraphy is
8 preserved in both cases and this is an important characteristic of rock avalanche
9 deposits.
- 10 3. The result of the filters on the 3D dataset is a colored point cloud where the slope
11 variations are assigned to a color scale. The method is fast and results into a rapid
12 mapping of the deposit.
- 13 4. The use of laser scanner and Structure from Motion are two different techniques to get
14 3D dataset. Both are valid and often they result to be complementary.
- 15 5. Even if the simulated roughness is not realistic compared to realistic conditions, it
16 gives good insight how the basal roughness influence the motion.
- 17 6. The analogue deposits present similar features as real cases events (Blackhawk and
18 Martian deposits, Figure 1).
- 19 7. The proposed methodology to map the deposit is fast, easy to use and cheap.

20 The application of the filtering technique on the deposit of the Frank Slide rock avalanches
21 gives encouraging results and after some further improvements could be applied in the future
22 to understand the dynamics of emplacement of historic rock avalanche observing interpreting
23 their deposit features.

24 **Acknowledgements**

25 The authors are grateful to P.-E. Cherix for the design of the laboratory setup and to Martin
26 Boesinger for his precious help in laboratory. The authors are also grateful to the Alberta
27 Geological Service for providing the data of the Frank Slide. Finally, many thanks to the
28 reviewers for the precious comments.

1 **References**

- 2 Adams, T., Grant, C., Watson, H.: Simple algorithm to relate surface roughness to equivalent
3 sand grain roughness, *Int. J. of Mechanical Engineering and Mechatronics*, 1, 2929-2724,
4 2012.
- 5 Andrade, S., D., van Wyk de Vries, B.: Structural analysis of the early stage of catastrophic
6 stratovolcano flank-collapse using analogue models. *Bull. Volcanol* 72, 771-789.2010.
- 7 Charrière, M., Humair, F., Froese, C., Jaboyedoff, M., Pedrazzini, A. and Longchamp. C.:
8 From the source area to the deposit: collapse, fragmentation and propagation of the Frank
9 Slide, *GSA Bull.*, 2015.
- 10 Cruden, D.M. and Hungr, O.: The debris of the Frank Slide and theories of rockSlide-
11 avalanche mobility, *Can. J. of earth Sc.*, 23,425-432, 1986.
- 12 Davies, T.R.: Spreading of rock avalanche debris by mechanical fluidization, *Rock*
13 *Mechanics*, 15, 9-24,1982.
- 14 Davies, T.R.H., and McSaveney, M.J.: Runout of dry granular avalanches, *Can. Geotech. J.*,
15 36, 313-320, 1999.
- 16 Davies, T.R.H., McSaveney, M.J.: Runout of rock avalanches and volcanic debris
17 avalanches,. *Proc. Int. Conf. on Fast Slope Movements*, Naples, 2, 2003.
- 18 Dufresne, A., Davies, T.R: Longitudinal ridges in mass movement deposits. *Geomorphology*
19 105, p. 171-181, 2009.Dufresne, A.: Granular flow experiments on the interaction with
20 stationary runout path materials and comparison to rock avalanche events. *Earth Surf.*
21 *Process. Landforms.*, 37, 14. 2012.
- 22 Dufresne, A., Prager, C., Bösmeier, A.: Insights into rock avalanche emplacement processes
23 from detailed morpho-lithological studies of the Tschirgabt deposit (Tyrol, Austria). *Earth*
24 *Surf. Process. Landforms* 41, 587-602. 2016.
- 25 Erismann, T.H.: Mechanisms of large landslides, *Rock Mechanics Felsmechanik*, 12(1),15-
26 46, 1979.
- 27 Francis, P.W., Gardeweg, M., O'Callaghan, L.J., Ramirez, C.F. and Rothery, D.A.:
28 Catastrophic debris avalanche deposit of Socompa volcano, north Chile, *Geology*, 14, 600-
29 603, 1985.
- 30 Friedman, S.J., Kwon, G. and Losert. W.: Granular memory and its effect on the triggering
31 and distribution of rock avalanche events, *J. of Geophysical Res.*, 108(B8), 1-11, 2003.

1 Gonzalez, R. C., Woods, R. E.: Digital Image Processing – Sec. Ed., Prentice-Hall, Inc., 2002.
2 Heim, A.: Der Bergsturz und Menschenleben. Fretz und Wasmuth Verlag, Zürich, 218 p.,
3 1932.
4 Hsü, K.J.: Catastrophic debris streams (strurzstroms) generated by rockfall, Geol. Soc. of Am.
5 Bul., 86, 129-140, 1975.
6 Hungr, O., Evans, S.G., Bovis, M., Hutchinson, J.N.: Review of the classification of
7 landslides of the flow type, Environ. Eng. Geosci., VII, 221–238, 2001.
8 Iverson, R.M., and Denlinger, R.P.: Flow of variably fluidized granular masses across three-
9 dimensional terrain I. Coulomb mixture theory, J. of Geophysical Res. B, Solid Earth,
10 106(B1), 537-552, 2001.
11 Kelfoun, K., and Druitt, T.H.: Numerical modelling of the emplacement of Socompa rock
12 avalanche, Chile, J. of Geophysical Res., 110, no. B12, 2005.
13 Kumar, L., Skidmore, A.K. and Knowles, E.: Modelling topographic variation in solar
14 radiation in a GIS environment, Int. J. Geo. Information Sc., 11,5, 475-497, 1996.
15 Locat P., Couture, R., Leroueil, S., Locat, J., Jaboyedoff, M.: Fragmentation energy in rock
16 avalanches, Can. Geotech. J., 43, 830-851, 2006.
17 Longchamp, C., Charrière, M. and Jaboyedoff, M.: Experiments on substratum roughness,
18 grainsize and volume influence on the motion and spreading of rock avalanches, Pan-Am
19 CGS Geotechnical Conference, 2001.
20 Longchamp, C.: The Propagation of Unconstrained Dry Granular Flows: from Laboratory to
21 Numerical Modelisation. PhD Thesis, University of Lausanne, Switzerland. 2016.
22 Manzella, I.: Dry rock avalanche propagation: unconstrained flow experiments with granular
23 materials and blocks at small scale, PhD thesis, EPFL, 2008,
24 Manzella, I., Labiouse, V.: Qualitative analysis of rock avalanches propagation by means of
25 physical modelling of not constrained gravel flows, Rock Mech. Rock Eng., 41 (1), 133–151,
26 2008.
27 Manzella, I., Labiouse, V.: Flow experiments with gravel and blocks at small scale to
28 investigate parameters and mechanisms involved in rock avalanches, Eng. Geol., 109, 146-
29 158, 2009.

1 Manzella, I., and Labiouse, V.: Empirical and analytical analyses of laboratory granular flows
2 to investigate rock avalanche propagation, *Landslides*, 10, no. 1, 23-36., 2013.

3 McDougall, S., and Hungr, O.: A model for the analysis of rapid landslide motion across
4 three-dimensional terrain, *Can. Geotechnical J.*, 41(6), 1084-1097, 2004.

5 Nicoletti, P.G., and Sorriso-Valvo, M.: Geomorphic controls of the shape and mobility of
6 rock avalanches, *Geol. Soc. of Am. Bul.*, 103(10), 1365-1373, 1991.

7 Paguican, E. M. R., van Wyk de Vries, B., Lagmay, A. : Hummocks : how they form and how
8 they evolve in rockslide-debris avalanches. *Landslides* 11. 67-80. 2014.

9 Pedrazzini, A., Froese, C.R., Jaboyedoff, M., Hungr, O., Humair, F.: Combining digital
10 elevation model analysis and run-out modeling to characterize hazard posed by a potentially
11 unstable rock slope at Turtle Mountain, Alberta, Canada. *Eng. Geol.*, 128, 76-94, 2012.

12 Pugazhenti, D., and Pria K.: A quantitative approach for textural image segmentation with
13 median filter, *Int. J. of Advancements in Res. & Tech.*, 2, Issue 4, 2007.

14 Scheidegger, A.E.: On the prediction of the reach and velocity of catastrophic landslides,
15 *Rock Mech. and Rock Eng.*, 5 (4): 231-236, 1973.

16 Shea, T. and van Wyk de Vries, B.: Structural analysis and analogue modeling of the
17 kinematics and dynamics of rockslide avalanches, *Geosphere*, 4, 657-686, 2008.

18 Van Gassen, W., and Cruden, D.M.: Momentum transfer and friction in the debris of rock
19 avalanches, *Can. Geotech. J.*, 26, 623-628, 1989.

20 van Wyk de Vries, B., Self, S., Francis, P.W., and Keszthelyi, L: A gravitational spreading
21 origin for the Socompa debris avalanche, *J. of Vol. and Geothermal Res.*, 105, p. 225–247.,
22 2001.

23 Westboy, M.J., Brasington, J., Glasser, N.F, Hambrey, M.J. and Reynolds, J.M.: “Structure-
24 from-Motion” photogrammetry: A low-cost, effective tool for geoscience applications,
25 *Geomorphology*, 179: 300-314, 2012.

26

1 Table 1. Characteristics of the used material.

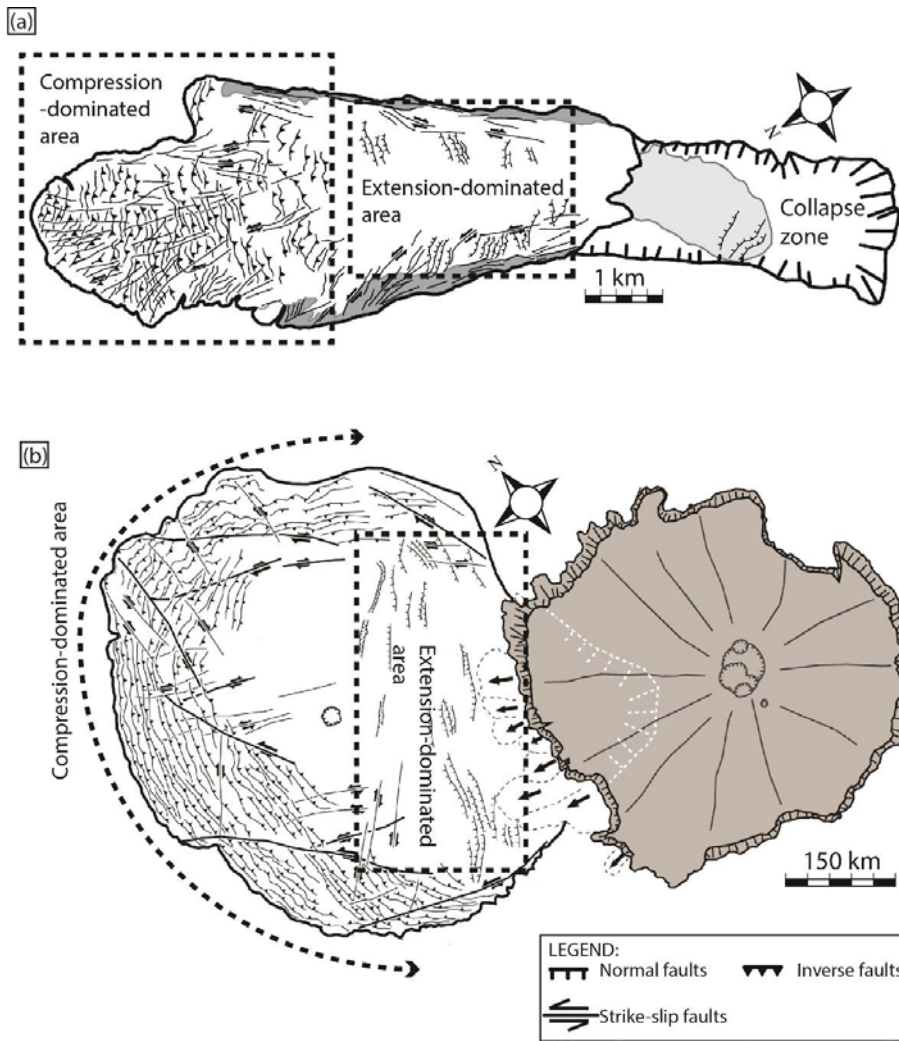
Grading		Mean grainsize(μm)	Range (μm).
Coarse	F10	2605	2830 - 2380
Medium	F36	545	590 - 500
Fine	F120	115	125 – 105
Colored	-	500	-

2

1 Table 2. Characteristics of the different substrata.

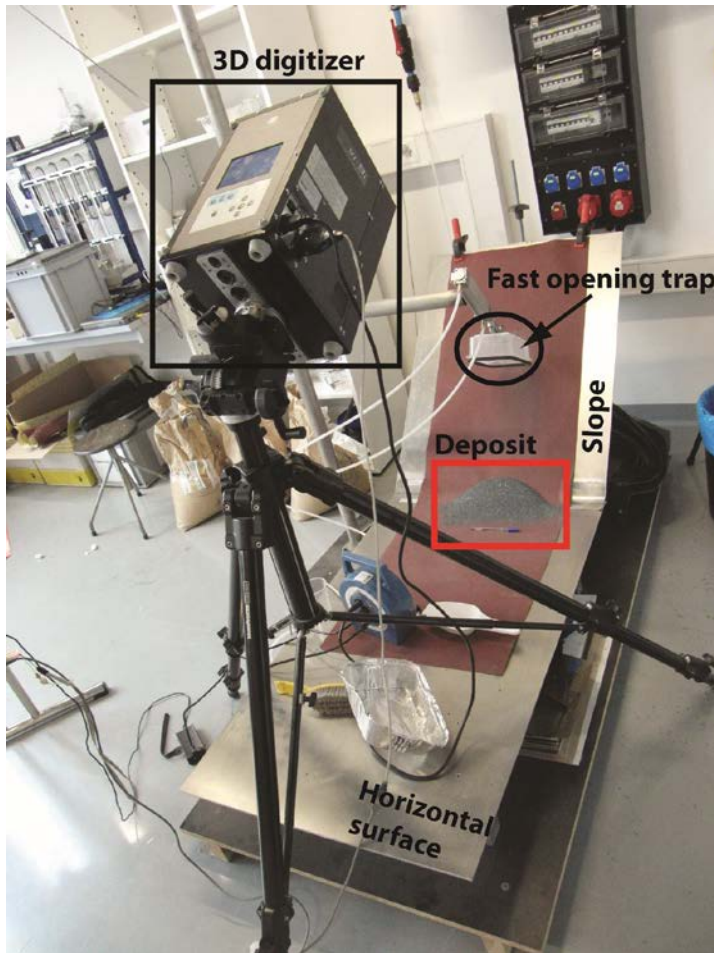
Sand	Grit	Grainsize (μm)	$\mu(^{\circ})$
Coarse	60	269	58.62
	120	125	48.67
Medium	320	46.2	43.17
	600	25.8	39.88
Fine	1200	15.3	34.13
	2500	8.4	33.40
Colored	-	42,5	44.79

2



1
2
3
4
5

Figure 1. (a) Blackhawk deposit and (b) Martian deposit (modified after Shea and van Wyk de Vries, 2008).

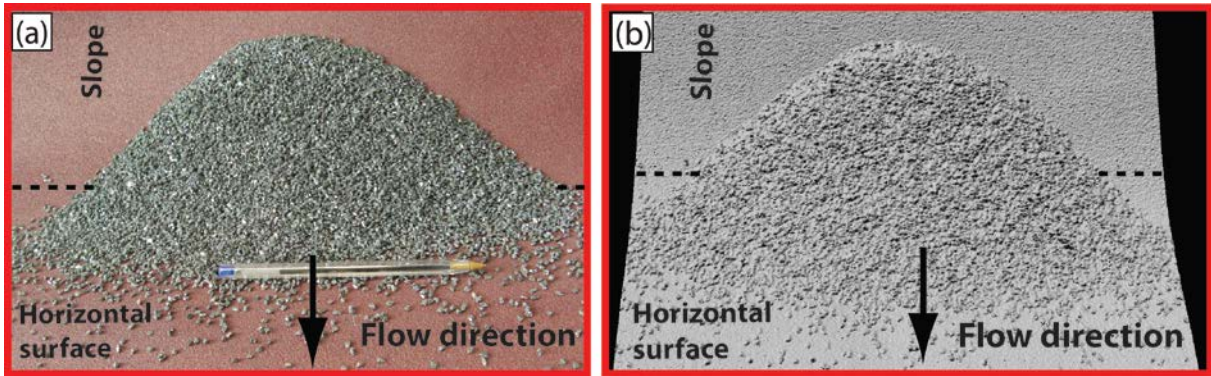


1

2

3 Figure 2. Laboratory setup.

4

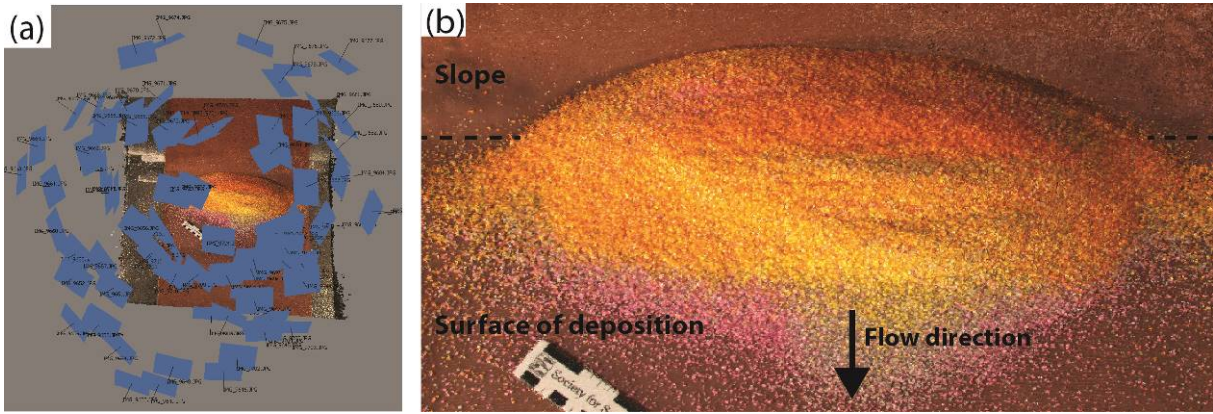


1

2

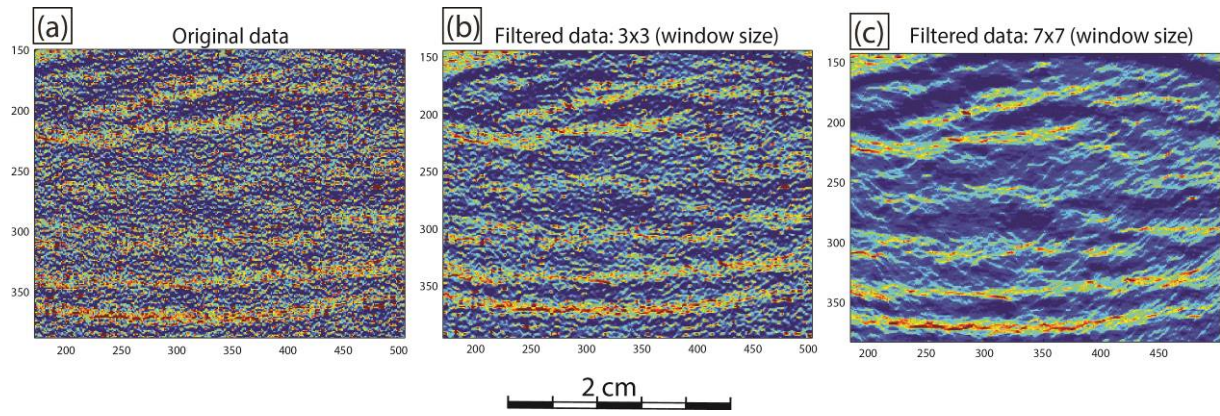
3 Figure 3: (a) Photography of a deposit of coarse granular material; (b) 3D model of the
4 deposit obtained by 3d laser scanning.

5



1
2
3
4
5
6

Figure 4: (a) View of the different position of the camera to take pictures for structure-from-motion; (b) 3D model obtained with structure-from-motion. Three colored sands were used for this experiment (yellow, grey, pink).

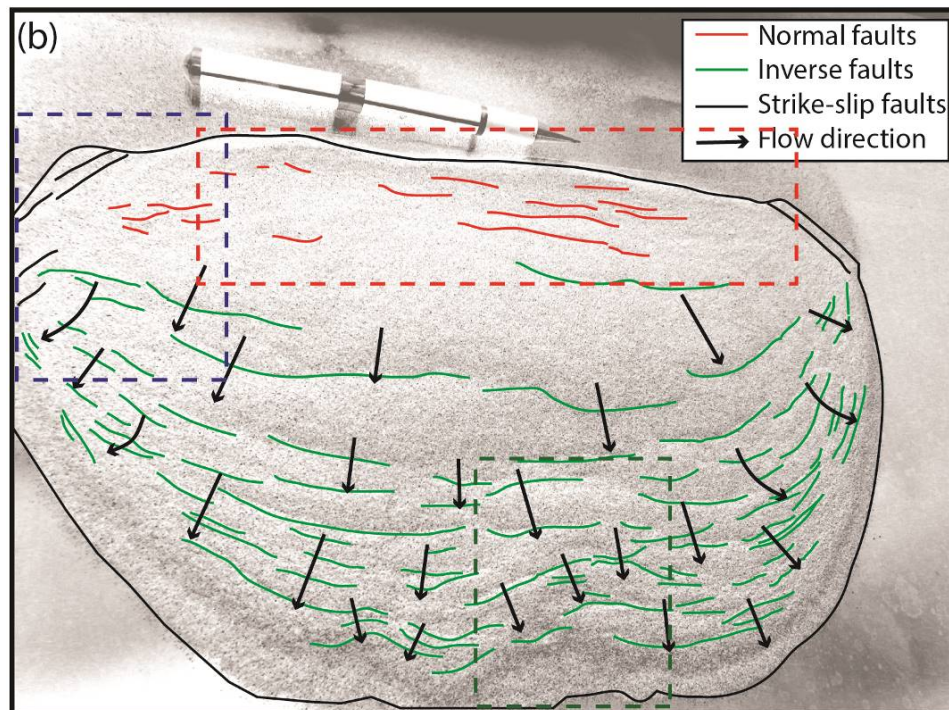
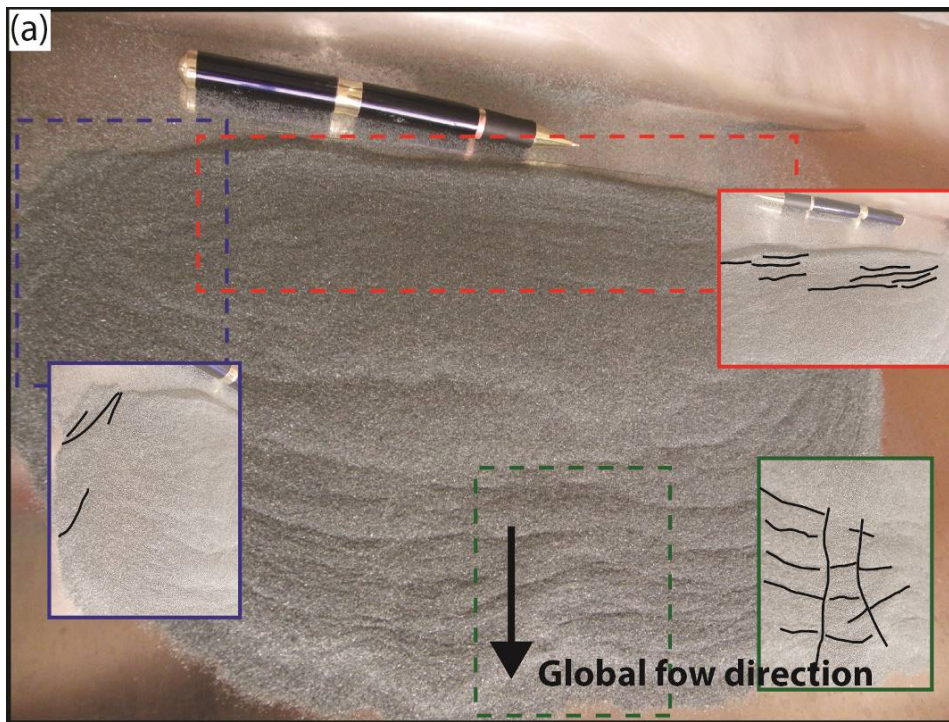


1

2

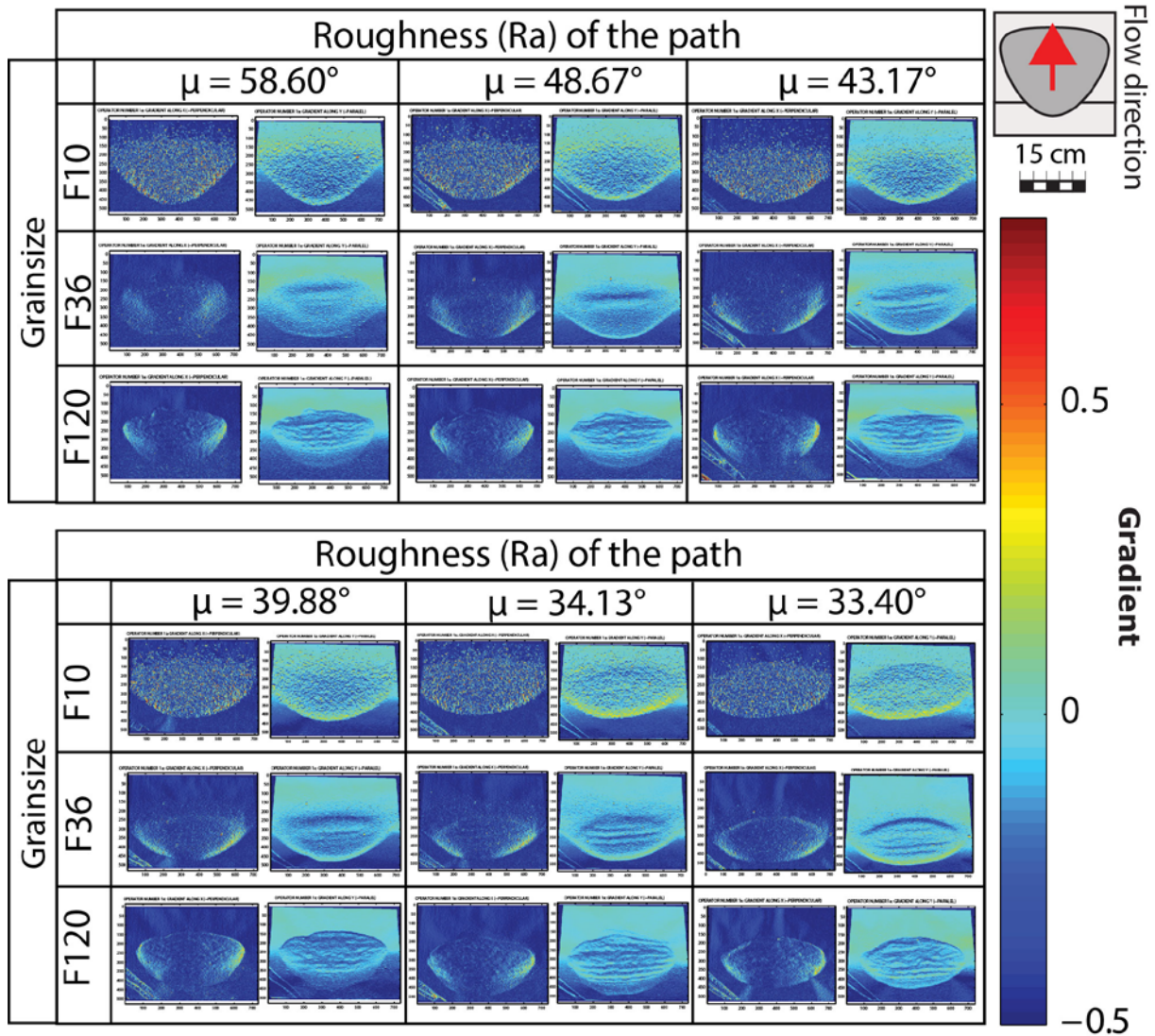
3 Figure 5: Application of the median filter to remove noises. (a) Original data; (b) Filtered
4 data; (c) with a 3x3 window size; (d) Filtered data with a 7x7 window size.

5



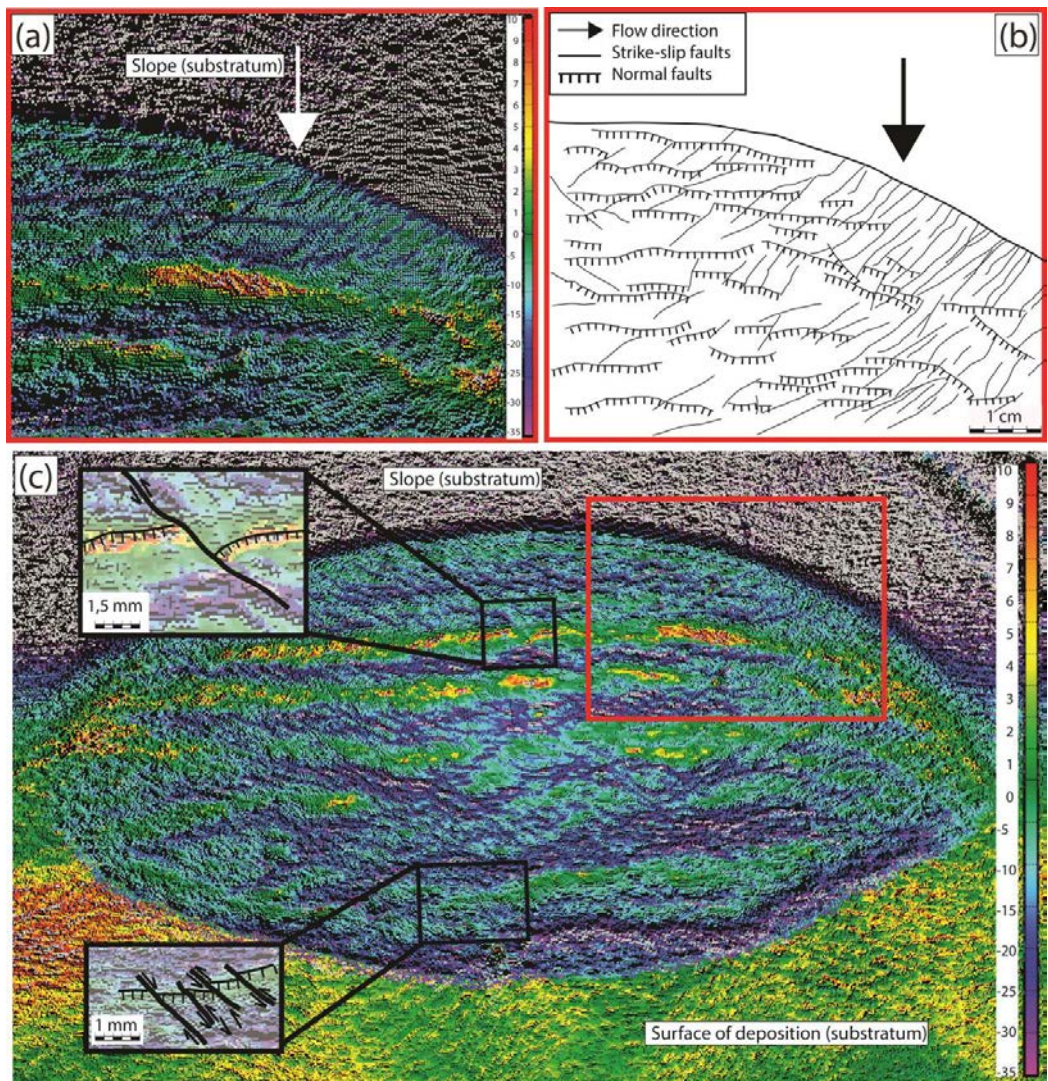
1
2
3
4
5

Figure 6: (a) analogue deposit (F120, aluminum substratum), view from the top; (b) result visual inspection and features mapping observed on the deposit surface.



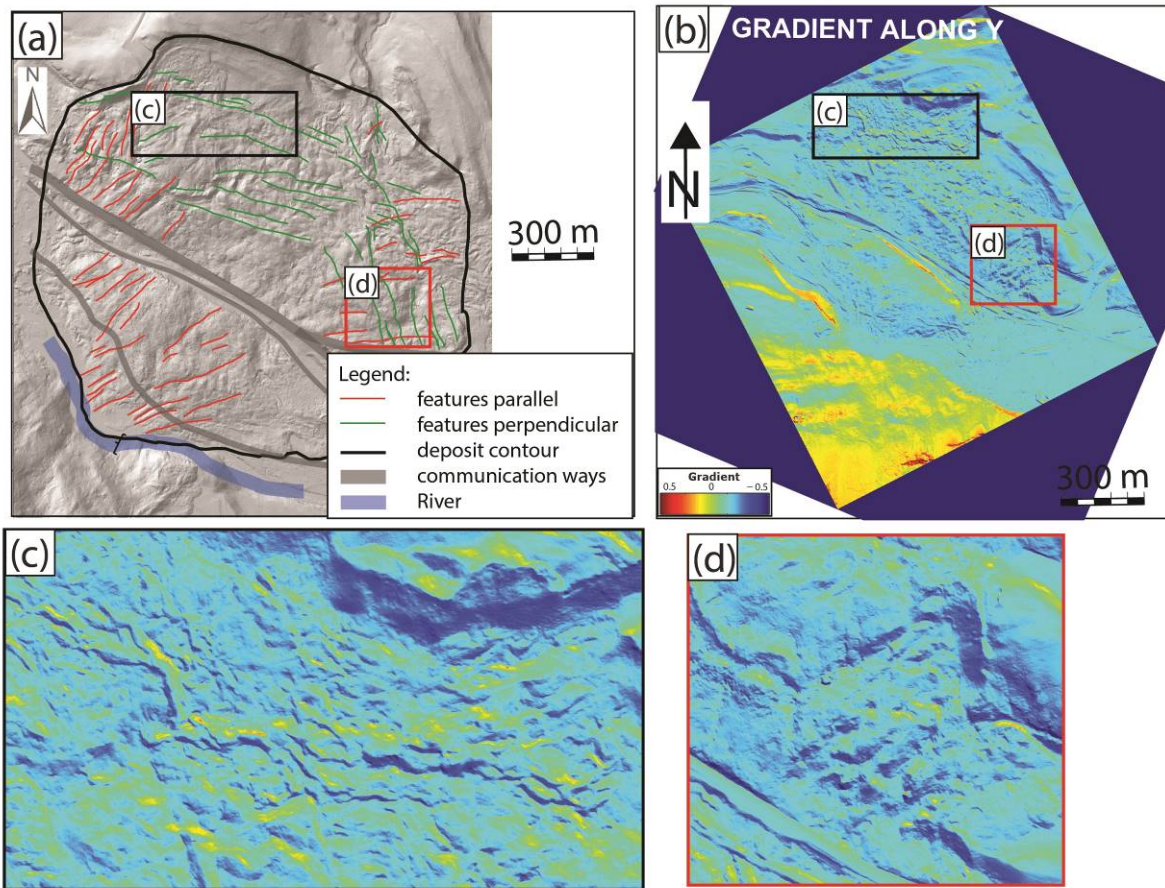
1
2
3
4
5
6

Figure 7: Results of the gradient along X and Y applied to all experiments carried for this research. The best results are obtained with the gradient along Y. The influence of the grainsize and the substratum on the shape of the deposit is clearly observable.



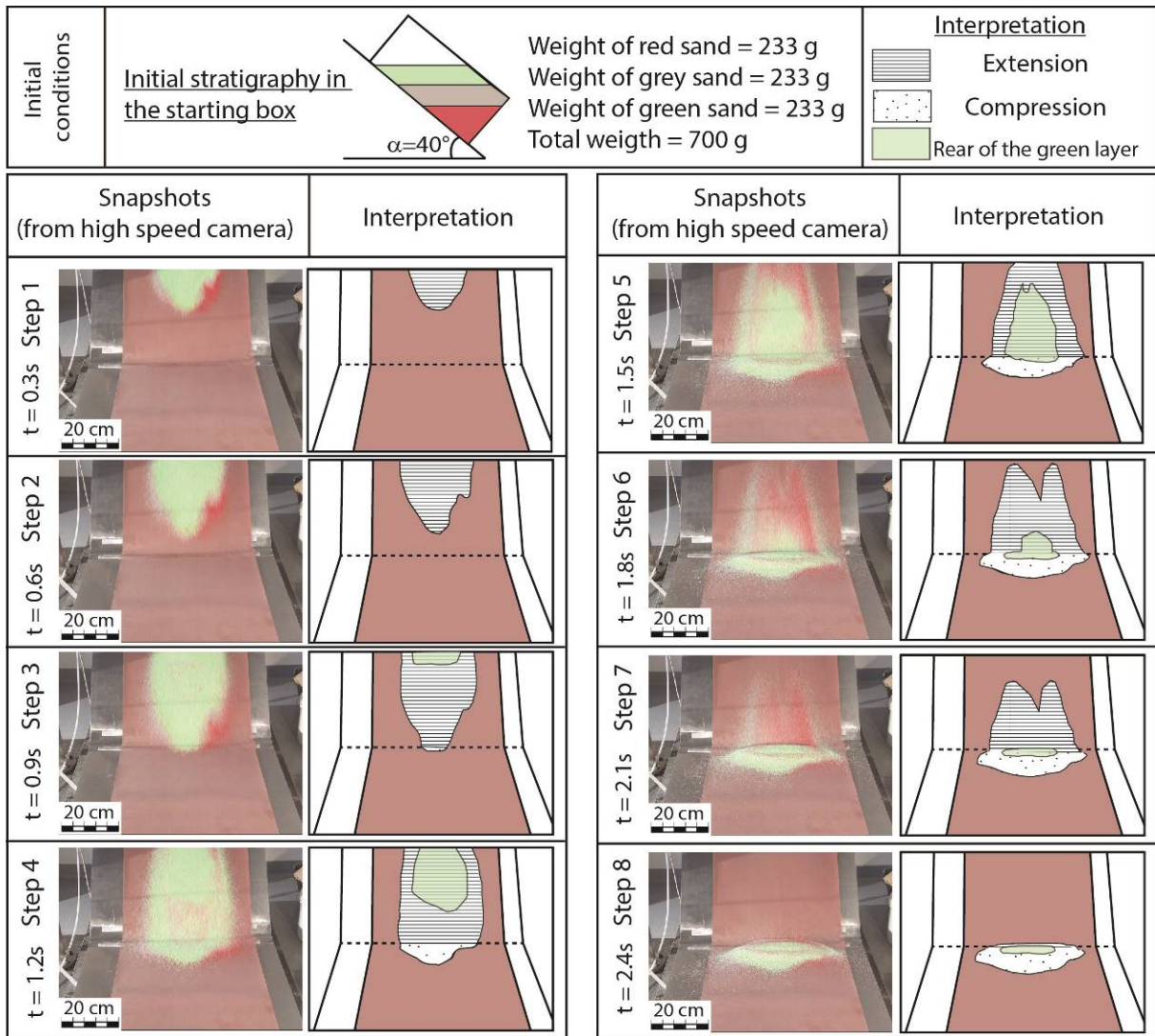
1
2
3
4
5
6

Figure 8: (a) Portion of the back of a deposit after post-processing and (b) detailed mapping of the back of the deposit. Strike-slip faults are numerous at the back, cutting normal faults.(c) the whole result.



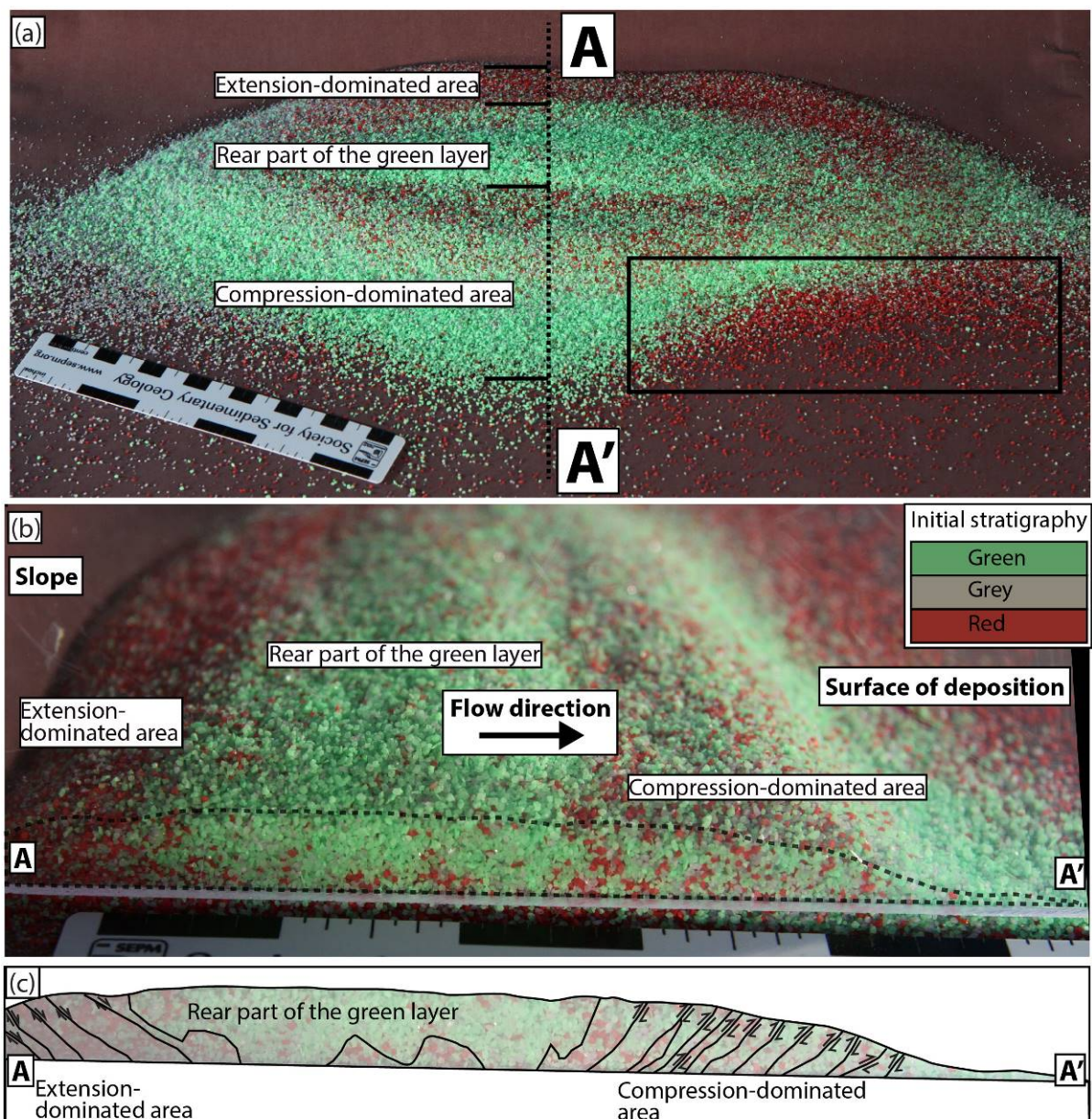
1
2
3
4
5
6

Figure 9: (a) Map of the different features observed on the DEM of Frank Slide deposit; (b) Result of the gradient along Y applied to the DEM of Frank Slide; (c) zoom on features perpendicular to the flow direction; (d) zoom on features parallel to the flow direction.



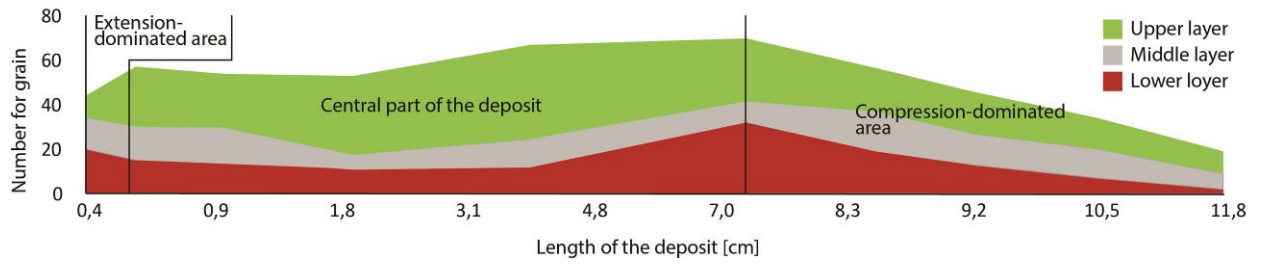
1
2
3
4
5
6

Figure 10: Time laps of an analogue granular flow (0.3 second between each picture). Three colored sand were used during this experiment (red, grey, green). On the left column are the snapshots of the experiment and the right column the interpretation of the flowing mass.



1
2
3
4
5
6

Figure 11: (a) analogue result of the experiment carried with 3 colored sands (Figure 10); (b) cross-section AA' through the center of the analogue deposit; (c) interpretation of the cross-section AA'.



1
2
3
4

Figure 12: repartition of the colored sand grains within the deposit.